Measurement 276 (2026) 121329

Contents lists available at ScienceDirect

Measurement

journal homepage: www.elsevier.com/locate/measurement

Experiment-based calibration of a digital twin for composite panel testing using standard signals

Raffael Bogenfeld [a,*], Tobias Wille [a], Oliver Witzel [b], Benjamin Eckstein [c], Christian Göpel [c]

[a] German Aerospace Center, Institute of Lightweight Systems, Lilienthalplatz 7, Braunschweig, 38108, Germany
[b] Carl Zeiss GOM Metrology GmbH, Schmitzstraße 2, Braunschweig, Germany
[c] Airbus Operations, Hamburg, Germany

ARTICLE INFO

Keywords:
Digital twin
Composite structures
Airframe
Structural testing
Model updating
Stiffened shell

ABSTRACT

Accurate assessment of composite structures depends on how experimental measurements are used to calibrate and validate numerical models. While nominal finite element models generally assume idealized conditions, actual manufactured components and test setups introduce notable uncertainties and require a tailored numerical representation. This paper presents a measurement-centric calibration framework that transforms a nominal finite element model into a specimen-specific Digital Twin using only standard test signals. The scalable methodology leverages nonlinear least squares optimization which is first demonstrated and verified on an analytical beam example, allowing for detailed investigation of convergence behavior as well as the improvements by parameter transformation and by Jacobian recalculation. Emphasis is placed on the linearization of model parameters prior to optimization and the role of measurement availability. This process significantly enhances calibration stability and accuracy. The method is then applied to a physical compression test of a stiffened CFRP panel at a subcomponent scale. Numerical studies are conducted to evaluate the sensitivity of the calibration process to parameter selection and validation metrics. Finally, a calibrated Digital Twin is created using experimental strain data and validated through the DIC-measured deflection field, demonstrating the model's ability to more accurately replicate the mechanical response of an individual composite panel.

1. Introduction

Efficient testing of a composite structure should extract as much information as possible while minimizing the effort required for preparation, testing, and evaluation. These capabilities allow the reduction of cost and time throughout the development process — both of which are crucial for maintaining competitiveness in industries that rely on lightweight composite structures, such as the manufacturing of aerospace structures. The qualification and certification procedures for aircraft structures still rely heavily on large-scale structural tests [1], even though modeling and simulation are becoming increasingly important for these tasks as outlined by Vetrano et al. [2]. To gain deeper insights into the mechanical behavior of a complex composite structure, a test-accompanying simulation is considered state-of-the-art. This often involves building a virtual test rig that embeds a detailed computational model of the physical specimen [3] and a numerical representation of the test setup. Typically, such numerical simulations rely on a nominal model representing the composite structure and the test rig as-designed.

To improve the accuracy of such test-accompanying simulations, the nominal model can be replaced by a Digital Twin, which digitally represents an actual physical specimen in a test rig. While the term “Digital Twin” first appeared in a NASA paper by Shafto et al. [4], Grieves formalized the development of the original Digital Twin idea in 2014 [5]. According to Grieves himself, the general Digital Twin concept dates back to 2002 [6], arising from an idea for product life cycle management. Nowadays, a Digital Twin is seen as a means of gaining competitive advantage, as summarized by Singh et al. [7], who outline the need for more efficient testing procedures. For example, in the aerospace industry, the Digital Twin technology is already well established, as Xiong and Wang explain in a comprehensive review article about Digital Twin applications for aviation [8]. Nonetheless, these authors conclude that the Digital Twin is mostly applied to manufacturing and maintenance in order to keep a digital copy updated throughout the structural life cycle.

Grieves [5] originally defined a Digital Twin as a “virtual representation of a physical product”. When we apply this concept over a

---

[*] Corresponding author.
E-mail address: raffael.bogenfeld@dlr.de (R. Bogenfeld).

https://doi.org/10.1016/j.measurement.2026.121329
Received 13 January 2026; Received in revised form 13 March 2026; Accepted 27 March 2026

Nomenclature

Index variables

c	compression
i	measurement data index
j	calibration parameter index
k	iteration loop index
m	total calibration parameters
n	total measured variables
ref	reference case as calibration target
t	tension

Material parameters

ν_{12}	Poisson's ratio
ρ	Mass density
E_{11}	Fiber direction modulus of a UD ply
E_{22}	Transverse direction modulus of a UD ply
G_{12}	Shear modulus of a UD ply
I	Second moment of area
K_{rot}	Rotational stiffness

Symbols

β	Calibration parameter
δ_{ij}	Kronecker delta
$\Gamma(x)$	Model in the physical domain
κ	beam curvature
$\mathbf{J}$	Jacobian matrix for nonlinear LSQ
$\mathbf{W}$	Weight matrix for weighted LSQ
$\tilde{F}(x)$	Linearized model derived from $F(x)$
$\tilde{y}_v$	Output data obtained from the linearized model
ε	Strain
F	Transverse beam load
$F(x)$	Model in the virtual domain
$I_\#$	Geometrical imperfection by eigenmode #
M	Bending moment
N	Normal beam load
$s_{\#E}$	Stiffness scaling factor for stiffener #
$s_{\#y}$	Lateral position for stiffener #
T	time period
u	beam elongation
w	Beam deflection
y_{ref}	Reference output data for calibration
y_v	Output data obtained from the model

product's life cycle, the virtual representation must be continuously updated to mirror any physical changes the product undergoes during its service life. In a typical workflow with a structural Digital Twin, as outlined by Jones et al. [9], the Digital Twin is created concurrently with the manufacturing of the physical structure and is updated throughout the structure's operational life. This process can even incorporate real-time data, aligning with the Digital Twin definition provided by Singh et al. [7]. Nevertheless, such updates usually rely on particular measurements (e.g., geometric dimensions). As a result, residual uncertainties may remain unquantified — for instance, those arising from the test configuration and measurement procedures. In contrast, we present a methodology that leverages in-situ experimental data to directly calibrate the Digital Twin, thereby capturing and compensating for these additional testing-induced uncertainties. Moreover, the structural assessment and the detection of damage by means of a Digital Twin are explored for various applications [10–12].

The authors of this paper introduce a Digital Twin framework specifically tailored to structural testing, in which a finite element (FE) model serves as the virtual counterpart to a physical test specimen (Fig. 1), following Bogenfeld's analogy of dual "spaces" [13]. We transform a nominal structural analysis model – our virtual space – into a fully calibrated Digital Twin by updating a defined set of parameters using data from the physical space. This interpretation of virtual space reflects Li et al.'s view of a Digital Twin as a specialized simulation method [14]. Our goal is to substantially improve the predictive accuracy of simulations conducted alongside physical tests. The proposed calibration strategy explicitly exploits the sensitivity of the measured signals to regression parameters, thereby linking measurement quality directly to model identifiability.

After theoretically deriving the calibration method as a nonlinear least squares optimization, we demonstrate the approach on a substructural composite panel test. Here, stiffness properties, geometric imperfections, and boundary-condition definitions, identified as the primary sources of uncertainty, are all treated as adjustable model parameters. To our knowledge, this is the first application of the Digital Twin concept in structural composite testing that leverages only standard experimental test signals for calibration. Unlike conventional workflows, which rely, for example on geometric measurements for a Digital Twin, our method also permits retrospective calibration of specimens already tested, which broadens the practical utility of Digital Twin in experimental structural investigations. Digital Twin realizations based on dense full-field measurements or detailed geometric re-scans can be effective, but they are instrumentation-intensive and rarely available in routine panel testing. To keep the instrumentation effort low, the present approach uses only standard test signals, supports post-test updating, and explicitly identifies boundary-condition stiffness, making Digital Twin calibration feasible for everyday structural investigations.

The novelty of this work lies in a measurement-driven calibration framework that generate a specimen-specific Digital Twin directly from standard signals obtained in a structural test. The approach exploits measurement sensitivity information through a Jacobian-based method and therefore explicitly links measurement quality to parameter identifiability. In contrast to conventional model updating approaches that primarily focus on numerical optimization, the proposed method emphasizes measurement-related aspects such as sensor relevance and measurement uncertainty. By integrating these aspects into the calibration process, the framework advances measurement-driven structural analysis and improves the reliability of simulation-based structural test evaluation.

2. Digital twin framework and calibration method

2.1. Requirements and definitions

The Digital Twin concept as illustrated in Fig. 1, relies on calibrating a virtual representation of a physical specimen leveraging data transferred from the physical domain into the virtual domain. The real model in the physical space represented by $\Gamma(x)$ acts as a reference whose results are denoted as $\Gamma(x) \rightarrow y_i^{ref}$ where $i \in [1..n]$ stands for a total of n measurement quantities. The independent variable x defines the state in both, the physical space and the virtual space. In our case x is typically a loading condition with one or more load amplitudes.

In the virtual space, a model corresponding to Γ has to be available. This virtual model $F(x)$ must provide the output quantities $F(x) \rightarrow y_i^v$ corresponding to those obtained in the physical space for a similar condition x. The preexistence of such a model is a requirement for the process established in this paper. In addition, the model must feature adjustable calibration parameters, denoted as β_j enabling the necessary model refinements. The Digital Twin shall be realized through a calibration procedure, during which an optimal set of parameters β_j^{twin} is

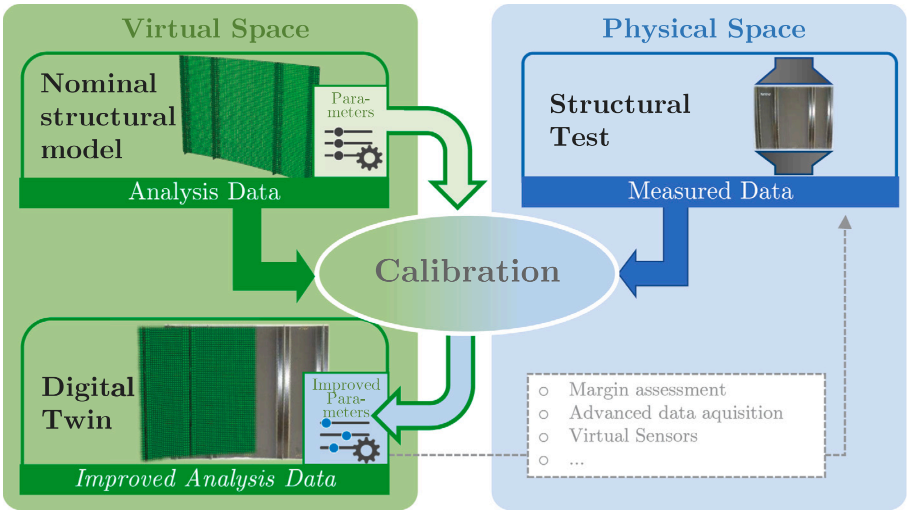

Fig. 1. Virtual space and physical space for the calibration of an Digital Twin analysis model for a structural test.

identified to best align the virtual model outputs y_i^v with the defined physical measurements y_i^{ref}.

Consequently, the calibration has to reduce the deviations Δ_i, defined according to Eq. (1) as the difference between measured physical test data and the corresponding analysis data in the virtual space. This calibration shall achieve the Digital Twin to more accurately reflect the unique characteristics of the individual structure in the physical domain.

$$\Delta_i = y_i^v - y_i^{ref} \tag{1}$$

The measurement data and the calibration parameters have the following properties:

1. The *measurement data* y_i which is to be matched between the physical and the virtual space. With a total number of n measured variables, $i \in [1..n]$. Each individual value y_i must be a scalar quantity. A measurement value can be any quantity that is recorded during a structural test. Typically, this would be either strain, displacement, or force (if not part of the set of independent variables x).
2. *Calibration parameters* β_j naturally exist only in the virtual space. With a total of m parameters is $j \in [1..m]$. Each individual parameter β_j has to be a scalar variable. Examples for such variables would be material parameters, geometric quantities, imperfections, or the stiffness at the model boundaries. Theoretically, any quantity that can be expressed as a scalar variable would be a suitable adjustment parameter.

2.2. Least squares approach

The objective of parameter optimization is to bring the analysis model $F(x)$, into the best possible agreement with the measured response of the physical model $\Gamma(x)$. The model agreement is measured through the result value mismatch Δ_i calculated through Equation (1). The difference Δ_i is zero if, at the considered measurement points, the descriptive model $F(x)$ no longer exhibits any discrepancies compared to the physical model $\Gamma(x)$.

To achieve the smallest possible deviations $\boldsymbol{\Delta}$, the regression parameters β_j are defined in the model $F(x)$, enabling various model adjustments where known uncertainties exist. Since the parameter set $\boldsymbol{\beta}$ is modified multiple times throughout the optimization procedure, multiple generations of regression parameters are created, denoted with the superscript k. Each generation of these regression parameters entails a new generation of result parameters, in accordance with Eq. (2):

$$F\left(x, \boldsymbol{\beta}^k\right) = \boldsymbol{y}^k \tag{2}$$

The parameter estimation method of least squares (LSQ) [15], which shall be employed in the optimization, is based on minimizing the squared deviations between the values computed by the model y_v and the known observation values y_{ref}, as shown in Eq. (3).

$$\min \left|\left|F(x, \boldsymbol{\beta}) - \Gamma(x)\right|\right|^2 = \min \left|\left|y_v - y_{ref}\right|\right|^2 \tag{3}$$

For the case of an arbitrary function $F_{linear}(x, \boldsymbol{\beta})$ depending linearly on all parameters in $\boldsymbol{\beta}$, the equation can be expressed in the form of a matrix operation, as shown in (4). The solution of the LSQ problem is expressed explicitly via matrix operations, as shown in Eq. (5).

$$F_{linear}(x, \boldsymbol{\beta}) = A\,\boldsymbol{\beta} \tag{4}$$

$$\hat{\boldsymbol{\beta}} = \left(\boldsymbol{A}^T \boldsymbol{A}\right)^{-1} \boldsymbol{A}^T \left(\boldsymbol{y} - g(x, \boldsymbol{\beta})\right). \tag{5}$$

This equation finds the optimal regression parameters $\hat{\boldsymbol{\beta}}$ in order to minimize the deviations between the function F_{linear} and the measurements $\boldsymbol{y}$. A single estimation yields the optimal solution of this linear problem. If the measurements $\boldsymbol{y}$ are in the codomain of $F_{linear}(x)$, it is even possible to obtain the exact values $\boldsymbol{\beta}^*$ such that $F_{linear}\left(x, \boldsymbol{\beta}^*\right) = \boldsymbol{y}$.

However, structures with a linear force–displacement response are unlikely to behave linearly with respect to the required adjustment parameters. Since the LSQ according to (5) is a linear method, directly substituting an arbitrary $F(x, \boldsymbol{\beta})$ is only possible if F is linear with respect to its parameters β_j. A possible linearity of F with respect to x is irrelevant here! If F depends nonlinearly on one or more β_j, a previous linearization of the function is necessary in order to perform the LSQ optimization. This linearization requires making use of the nonlinear LSQ method [16] solving Equation (3) iteratively.

2.3. Nonlinear least squares

In order to apply the LSQ estimation method to a nonlinear problem, one must linearize the objective function which is achieved by a first-order Taylor series expansion [17] at the base point β^0, according to Eq. (6). This first-order Taylor approximation results in the linearized function as $\tilde{F}(x, \boldsymbol{\beta}) = \tilde{y}_v$.

$$\tilde{F}^0(x, \beta) = F\left(x, \beta^0\right) + \left.\frac{\partial F}{\partial \beta}\right|_{\beta^0} \left(\beta - \beta^0\right) \tag{6}$$

Eq. (6) is linear with respect to the regression parameters $\boldsymbol{\beta}$, or more precisely, with respect to the parameter difference $\Delta\beta = \left(\beta - \beta^0\right)$. The matrix $\boldsymbol{J}$ resulting from the derivative $\partial \boldsymbol{F} / \partial \boldsymbol{\beta}$ contains the gradients of each result value $y_i = F_i(x, \boldsymbol{\beta})$ with respect to each parameter β_j at the initial base point β^0, as shown in Eq. (6).

$$J^0_{i,j} = \frac{\partial F_i}{\partial \beta_j}\bigg|_{\beta^0} \tag{7}$$

The gradient matrix $\boldsymbol{J}$ [16], also called the Taylor matrix or sensitivity matrix, is the Jacobian $\boldsymbol{J}^0_{n\times m}$ of the nonlinear objective function F, and it contains, column by column, the gradients of all n measured values for each of the m regression parameters.

To compute these gradients for a case where F is a numerical simulation model, the partial derivatives $\frac{\partial F}{\partial \beta}$ cannot be analytically obtained. The Jacobian in Eq. (7) therefore has to be expressed as a difference quotient given in Eq. (8).

$$J^0_{i,j} = \frac{F_i^{0+\Delta\beta_j} - F_i^0}{(\beta_j^0 + \Delta\beta_j) - \beta_j^0}\Bigg|_{\beta^0} = \frac{F_i^{0+\Delta\beta_j} - F_i^0}{\Delta\beta_j}\Bigg|_{\beta^0} \tag{8}$$

Leveraging the linear gradients, the approximation function $\tilde{F}$ in Eq. (6) allows us to proceed with the linear LSQ algorithm. The corresponding optimization condition is given by Eq. (9) which is solvable analogously to (5).

$$\min \left|\left|\tilde{F}(x, \boldsymbol{\beta}) - y_{ref}\right|\right|^2 \tag{9}$$

To express the linearized function $\tilde{F}(x, \boldsymbol{\beta})$ as a single matrix operation, we replace the regression parameters $\boldsymbol{\beta}$ with $\Delta\beta = (\boldsymbol{\beta} - \boldsymbol{\beta}^0)$. We also rewrite the function as $\tilde{F}(x, \boldsymbol{\beta}) = F\left(x, \boldsymbol{\beta}^0\right) + J^0\,\Delta\boldsymbol{\beta}$, leading to the optimization problem given by Eq. (10)

$$\min \left|\boldsymbol{J}^0\,\Delta\boldsymbol{\beta} - \left(y_{ref} - F\left(x, \boldsymbol{\beta}^0\right)\right)\right|^2 \tag{10}$$

Since the initial values $F\left(x, \beta^0\right)$ are known, one obtains the solution of the linearized LSQ problem in Eqs. (11) and (12), where the latter provides an updated data set β^1. This data set is not the final solution, since the nonlinear target function $F(x)$ does not allow obtaining a best-fit solution in one step.

$$\Delta\hat{\beta} = \left(\boldsymbol{J}^{0^T}\boldsymbol{J}^0\right)^{-1}\boldsymbol{J}^{0^T}\left(y - F\left(x, \boldsymbol{\beta}^0\right)\right), \tag{11}$$

$$\boldsymbol{\beta}^0 + \Delta\hat{\boldsymbol{\beta}}\cdot\xi = \boldsymbol{\beta}^1. \tag{12}$$

Hence, the nonlinear LSQ optimization has to be established as an iterative process as shown in Fig. 2. After the calculation of an improved set of parameters, a new set of result values y_v^1 is obtained from the accordingly updated model $\tilde{F}(x, \beta^1)$. A fully correct iteration would require to recalculate a new Jacobian $\boldsymbol{J}^1$, (cf. the path "iterated Jacobian" in Fig. 2) as the gradients also depend on the regression parameters themselves. However, as the calculation of the Jacobian is the most computationally expensive step, for large models it is computationally more efficient to iterate using the initial Jacobian $\boldsymbol{J}^0$. That way, the new values differences $y_{ref} - F(x, \beta^1)$ are calculated, from which the next iteration loop can begin. The iteration can be terminated based on several cut-off criteria, such as achieving a predefined tolerance in the result values, a threshold value for the changes in the regression parameters or a fixed number of allowed iterations k_{end}. The model $F(x, \beta^k)$ of the final iteration is considered the Digital Twin that is obtained through this process.

The slowness parameter ξ limits the allowable $\Delta\hat{\beta}$ in one iteration in order to prevent overshooting for nonlinear response. While its upper limit is 1, its ideal value depends on the number of iterations, typically around 0.5. If an increasing sum of squared residuals is observed during the optimization, the parameter ξ is reduced for both the current and the iteration cycles.

2.3.1. *Computational effort*

The total computational effort of the calibration process in Fig. 2 depends on the numerical run time of the analysis model T_m as the optimization loop includes one numerical analysis with the updated parameter set in each iteration. In addition, the calculation of the Jacobian according to Eq. (8) requires one perturbed analysis for each regression parameter β_j. One perturbed simulation $F^{0+\Delta\beta_j}$ provides all n result values to calculate the column j of the Jacobian through the finite-difference method (Eq. (8)). If the Jacobian matrix is recomputed at each iteration, the total required time T_{total} is dominated by the product of T_m, the number of parameters m, and the total iterations k_{end}, as given by Eq. (13).

By using the initial Jacobian matrix J^0 throughout all iterations, the most expensive step is removed from the iteration loop, significantly reducing computational effort. According to Eq. (14), the reduced computation time $T_{\text{total}-J^0}$ becomes the multiple of T_m and the sum of the number of parameters m and the number of iterations k_{end}.

$$T_{total} = T_m \cdot \left(1 + (m+1)\cdot k_{end}\right) \tag{13}$$

$$T_{total-J^0} = T_m \cdot \left(1 + m + k_{end}\right) \tag{14}$$

2.4. *Parameter preparation*

Even the nonlinear LSQ estimation is able to determine an exact solution, if the target function is linear and the reference result values y_{ref} are in the function F's codomain. For a nonlinear problem, the linear Taylor approximation facilitates quickly finding an optimal solution, as long as the original nonlinear function F does not deviate too far from its local linear approximation and that the gradients given by the Jacobian do not change too severely. This advantage can be enhanced through an *a priori* parameter transformation. Each calibration parameter can be converted into a quantity affecting the result in a linear way.

For example, in the one-dimensional Hooke's Law given in Eq. (15), where N_1 is a force and A is the cross sectional area calculated from a thickness h and a width b, we can treat the Young's Modulus E an uncertain parameter which we want to improve through a regression based on a strain measurement. While the strain ε is nonlinear with respect to E, it is linear with respect to the inverse $\frac{1}{E}$. Therefore, using $\frac{1}{E}$ as the calibration parameter is more suitable for the LSQ method. Similar parameter transformations can be found for other typical parameters in structural equations. For a bending problem of a rectangular beam (width b and thickness h, cf. Section 4.1) loaded with a moment M_1, the measurable strain ε would be proportional to $\frac{1}{h^3}$. In this case, using $\frac{1}{h^3}$ as a calibration parameter is more appropriate than using the thickness h directly.

$$\varepsilon = \frac{N_1}{EA} = \frac{N_1}{Ebh} \tag{15}$$

$$\varepsilon = \frac{M_1}{EI} = \frac{12\cdot M_1}{Ebh^3} \tag{16}$$

Both these Eqs. (15) and (16) allow us to deduce generalized findings regarding the linearization of stiffness and geometric parameters. In particular, the influence of any stiffness quantity can be linearized via inversion, provided the measured values are strains or displacements. However, the effect of the thickness h appears as a first-order term in Eq. (15) but as a third-order term in Eq. (16), so a perfect linearization for h is not achievable for a combined load case.

2.5. *Calibration strategy and reference variable*

In structural testing, Digital Twin calibration seeks to minimize the discrepancy between experimental observations and numerical predictions. Two basic strategies are available. The first is a *point-based* calibration performed at a single, representative load level; the second

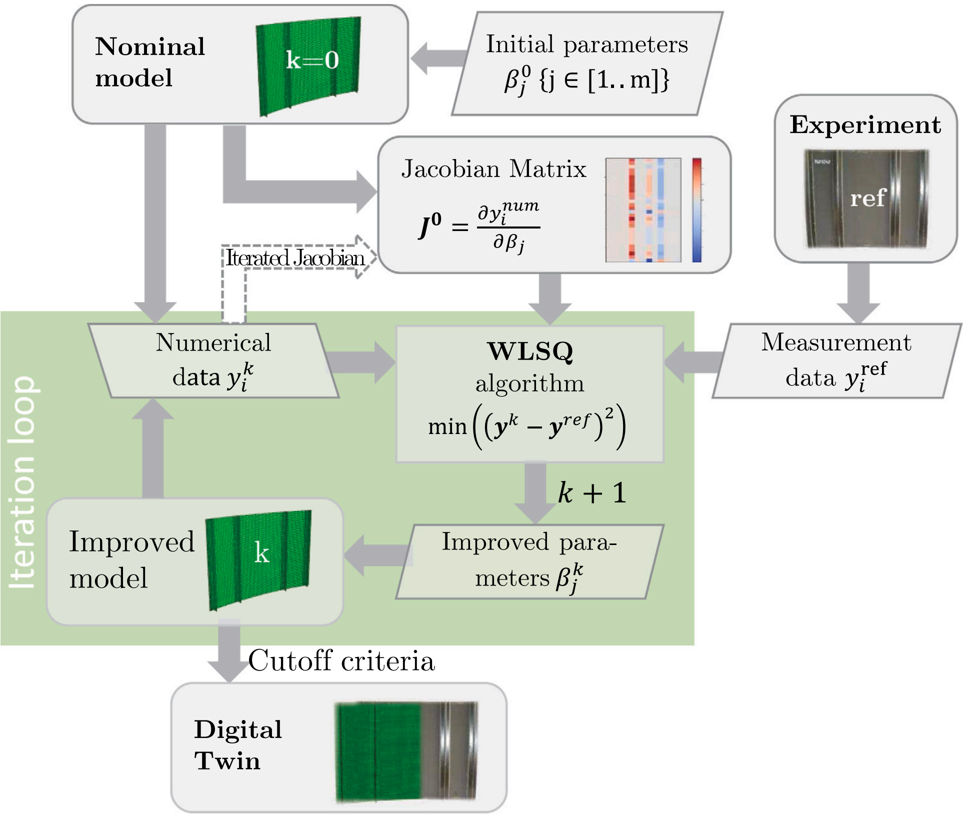

Fig. 2. Process of the iterative calibration through the weighted least squares algorithm.

is a *curve-based* approach that exploits the entire load–displacement history. Although the latter may furnish additional information, it also amplifies the influence of unmodeled nonlinearities and measurement noise at low load levels.

A curve-based calibration is beneficial to identify parameters that govern strongly nonlinear behavior. For example, progressive damage, plasticity, or buckling phenomena. In such cases, the full load history improves parameter separation. A point-based calibration may even be insufficient could lead to a nonphysical parameter update.

In the present study, however, the calibrated parameters primarily influence stiffness and boundary conditions within a load range free of global buckling or structural degradation. The selected calibration point lies in a stable response regime. Including the entire load history would therefore provide limited additional identifiability while increasing sensitivity to measurement noise and settlement effects.

Nonetheless, the proposed framework is not restricted to single-point calibration and can be extended to multi-point or curve-based objectives when nonlinear parameter identification is required.

The independent variable used to define the calibration point must be selected with care. Displacement readings are often affected by compliance in the load path, so matching the model to a prescribed displacement can introduce systematic error. We therefore choose the externally applied load – expressed in terms of axial force and, where applicable, bending moment – as the reference quantity. When the numerical model reproduces the measured forces and moments at the chosen load level, the physical and virtual boundary conditions can be regarded as equivalent, providing a robust foundation for subsequent parameter identification.

It should be noted that the calibration does not assume prior knowledge of the true specimen parameters. Instead, the optimization starts from β^0, a nominal parameter set, typically derived from design values, geometric measurements, or engineering assumption if no nominal data is obtainable. The Jacobian matrix $\boldsymbol{J}$ is evaluated at this initial configuration β^0. For efficiency reasons, $\boldsymbol{J}$ may be kept constant throughout the iterative optimization.

The validity of this approximation depends on the magnitude of the parameter updates and on the degree of nonlinearity in the response of F with respect to the updated regression parameters. If stronger nonlinear effects are expected or if the optimization does not converge, the Jacobian can be recomputed iteratively without modifying the underlying framework.

The proposed strategy is not restricted to the present panel application. It is generally applicable to parameterized FE models, provided that the selected measurements exhibit sufficient sensitivity to the chosen calibration parameters.

2.6. Weighted LSQ accounting for sensitivity

Depending on the problem definition, not all measurements are equally sensitive to the calibration parameters. Some measurement values may be only weakly affected by the parameter adjustments because their deviation is caused by unknown mismatches between the model and the real specimens. These unknown aspects might be not captured by the chosen regression parameters. The calibration method has to ensure that the optimization does not excessively manipulate the regression parameters in order to match such parameters. This would be overfitting.

This can be achieved through a weighted least squares (WLSQ) approach [18], where the weights in the diagonal matrix $\mathbf{W}$ are calculated as the norm of the rows from the Jacobian matrix $\|\boldsymbol{J}^0_{i,:}\|_2$. The weighted LSQ approach leads to a modification of Eq. (11) into Eq. (17) where $\mathbf{W}$ is defined by Eq. (18) with δ_{ij} denoting the Kronecker delta. The weight term in the LSQ estimation has no noticeable influence to the computational effort.

$$\Delta\hat{\beta} = \left(\boldsymbol{J}^{0^T}\,\boldsymbol{W}\boldsymbol{J}^0\right)^{-1}\boldsymbol{J}^{0^T}\boldsymbol{W}\left(y - F\left(x, \beta^0\right)\right) \tag{17}$$

Table 1
Nominal material data for Hexcel M91 unidirectional prepreg with a IM7 fiber reinforcement according to the data sheet [19] and Dienel 2019 [20].

Parameter	Value
E_{11t}	165 GPa
E_{11c}	150 GPa
E_{22t}	8.5 GPa
E_{22c}	8.6 GPa
G_{12}	5.5 GPa
ν_{12}	0.3
t_{ply}	0.184 mm
ρ	1570 kg/m^3

$$\boldsymbol{W}_{ij} = \delta_{ij} \|\boldsymbol{J}^0_{i,:}\|_2, \quad 1 \leq i, j \leq n \tag{18}$$

3. Experimental setup and test scenario

3.1. Stiffened composite compression panel

A stiffened composite panel featuring four longitudinal stiffeners was experimentally tested under uniaxial compression loading.

The test article depicted in Fig. 3(a) is a curved CFRP panel stiffened by four T-stiffeners. The skin has a curvature radius of 2075 mm, an arc length of 800 mm, and a total height of 653 mm. Two stiffeners are placed directly at the panel edges, where the end of the stiffener foot aligns with the panel edge. The stiffeners partition the panel such that the arc distance between neighboring stiffeners is 185 mm, except for the central bay between stiffeners 2 and 3, which is twice as wide 370 mm.

The strain measurement locations for the compression test are shown in the technical sketch in Fig. 3(b). Back-to-back strain gauges are applied to the panel at each measurement location.

The skin 4 mm laminate has a symmetric stacking sequence $[45_3, 0, -45_3, 90, -45, 0, 45]_s$, constructed from Hexcel M91 [19] unidirectional prepreg with IM7 fiber reinforcement (ply thickness $t_{\mathrm{ply}} = 0.184$ mm). This configuration is similar to the laminate configuration of the coupon tests investigated by Dienel [20] and by Bogenfeld et al. [21]. Nominal material data is given in Table 1.

Each T-stiffener has a web height of 32 mm and a foot width of 28 mm to both sides. The stiffener foot uses the 7-ply layup $[45, 0, -45, 90, -45, 0, 45]$ and the stiffener web uses a symmetrical 21-ply layup with a 0 degree center ply $[45, 0, -45, 90, -45, 0, 45, 45, 0, -45, \underline{0}]_s$. All plies are taken from the same M91/IM7 system as for the skin. This configuration yields a representative curved, stiffened panel with well-defined geometry and stacking sequences for subsequent calibration and validation.

3.2. Experimental setup and procedure

The panel was tested in the buckling test machine of the Institute of Lightweight Systems of the German Aerospace Center, which is described by Wilckens et al. [22] and Degenhardt et al. [23]. The hydraulic machine, with an axial compression load capacity of 1000 kN, is suitable for quasi-static or cyclic testing of panel and cylinder specimens. Fig. 4(a) shows the panel mounted inside the test machine. The fixation of the panel ends in the machine is realized through resin blocks embedding each panel end over a height of 60 mm. These resin blocks enable load introduction and constrain rotation of the panel ends. The free length of the panel is defined as the remaining height between the resin blocks and measures 533 mm.

In a displacement-controlled test with a constant loading rate of 0.15 mm min^{-1}, axial compression load was applied up to 271 kN, which corresponded to a crosshead displacement of 0.77 mm and a nominal strain level of 1444 $\mu\varepsilon$.

Test data were recorded from the test machine (axial force measured by the integrated load cell of the test frame and crosshead displacement), optical measurements using the stereo camera system (ARAMIS [24]) on both skin surfaces, and 40 quarter bridge-strain gauges arranged in a back-to-back configuration on the skin and the stiffeners. Two displacement transducers on both ends of the panel were used to measure the axial shortening over the panel's total length. Displacement, strain, and force signals were recorded at a sampling rate of 5 Hz. DIC data from the ARAMIS was recorded with a sampling rate of 0.2 Hz.

3.3. FE simulation model

An FE surface model as shown in Fig. 5 was constructed using four-node linear shell elements (S4R) for both the skin and the stiffeners. The element edge length was approximately 8 mm, resulting in approximately 66 elements over the free test length in axial direction.

Each T-stiffener was represented by two distinct shell surfaces (foot and web). The stiffener foot was tied to the skin, and the web was tied to the foot, using tie constraints to enforce compatibility across the interfaces. Composite laminate sections were assigned to the skin, stiffener foot, and stiffener web to reproduce the stacking sequences specified above. The material behavior was assumed to be linear elastic and orthotropic, with stiffness properties defined according to Table 1. Geometric nonlinearity was activated to account for second-order deformation effects. A degradation model or failure criterion was not implemented, as the investigated load range did not involve global buckling or damage initiation/propagation.

The boundary conditions follow the general description of the panel test configuration provided by Wilckens et al. [22]. Transverse displacements at both panel ends were constrained, while axial compression was applied at the lower boundary. According to Wilckens, the rotational boundary conditions around the panel edge axes are often idealized as fully clamped in comparable panel tests. However, a sensitivity analysis conducted in the present study showed that neither a purely clamped nor a simply supported representation reproduces the panel response adequately.

Fig. 4(b) illustrates the influence of the idealized boundary conditions on the predicted strain on both sides at the upper panel end. Neither a clamped nor a simply supported configuration reproduces the experimental strains. Therefore, the rotational boundary condition was modeled using an elastic rotational spring with stiffness $Krot$ to represent the compliance of the resin embedding at the panel ends.

Global buckling eigenmodes depicted in Fig. 5 were obtained from a linear perturbation analysis in a buckling eigenvalue analysis step, from which the first three eigenmodes were extracted. The eigenmodes show buckling pattern featuring two or three buckles with major out-of-plane displacements in the central bay of the panel. A behavior that is caused by the increased width of the central bay compared to the two outer bays.

The compression load was then applied in a subsequent `*STATIC` step. The displacements obtained from the buckling analysis were introduced as initial geometric imperfections via the `*IMPERFECTION` keyword by seeding each buckling eigenmode with a small prescribed amplitude. This technique is known as the eigenmode-affine method and adopted by many researchers [25–27]. Its suitability to predict deformation under compression load is well acknowledged.

The resin end blocks were not modeled. Instead, the FE model represents only the free length of the panel, 533 mm in the z-direction, omitting the embedded length. Boundary and loading conditions were applied at the reduced panel ends representing the transitions to the resin blocks, thereby eliminating rigid-body motions and providing the resultant axial compression while avoiding the unknown stiffness contribution from the resin embedding.

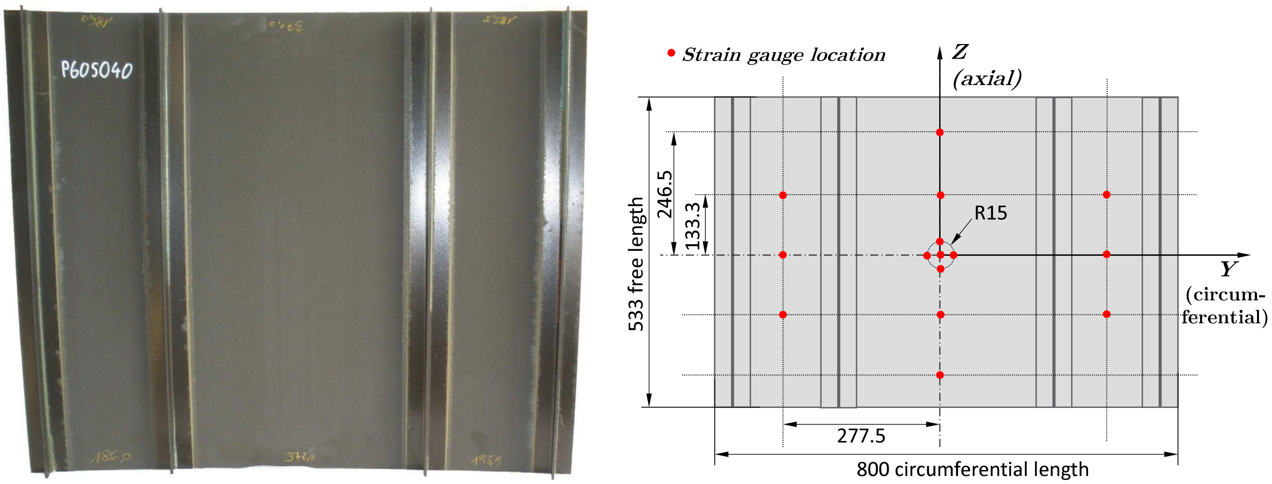

(a)

(b)

Fig. 3. (a) Manufactured 4-stringer CFRP panel specimen for the compression test (b) Technical sketch of the panel showing dimensions and strain gauge positions.

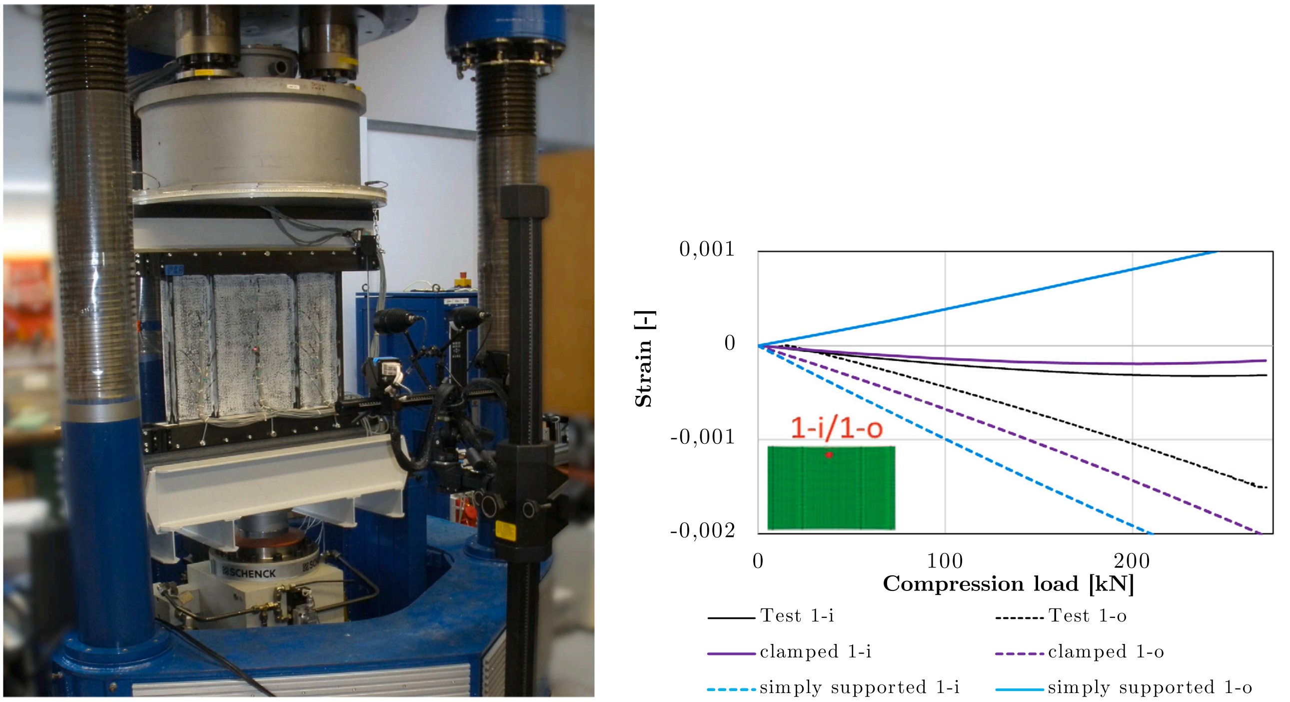

(a)

(b)

Fig. 4. (a) Experimental setup for the panel compression test. (b) Strain response at the measurement point 1 in the test compared to simulations with simply supported and clamped boundary conditions.

3.4. Model uncertainties and calibration parameters

There are different sources of uncertainty relevant to calibrating the Digital Twin that represents the actual test specimen. Regarding the test procedure, the boundary conditions in the test machine are a notable source. The resin embedding at the panel end imposes elastic boundary conditions between fully clamped and simply supported. Its effective stiffness toward rotational deformation is unknown and can be estimated to achieve an accurate representation. An initial rotational stiffness of $100\,\mathrm{kN\,mm\,rad^{-1}}$ was defined, representing an engineering estimate of the boundary stiffness which was based on preliminary simulations.

With regard to the specimen itself, geometrical uncertainties can significantly affect the structural response. The eigenmode-affine simulation approach that parameterizes the geometric imperfections as a linear combination of the buckling eigenmodes does not necessarily reproduce the specimen's real geometric shape. Hence, the eigenmode-affine imperfection can be calibrated through the scaling factors I_1, I_2, and I_3 for each mode.

Furthermore, the material properties exhibited uncertainties, especially the longitudinal modulus E_{11}, due to a $10\,\%$ discrepancy between compression and tension moduli shown in Table 1. In addition, the shear modulus G_{12} must be considered carefully, since the actual shear response of a composite is highly nonlinear, as demonstrated by typical

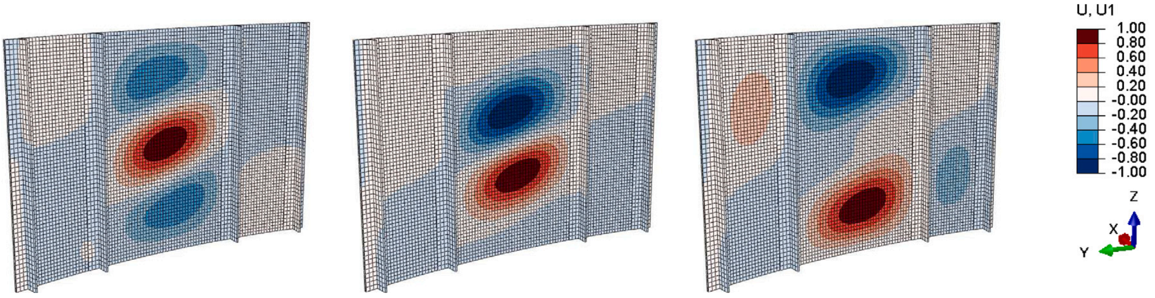

Fig. 5. FE model showing the normalized x-direction displacements of the first three buckling eigenmodes.

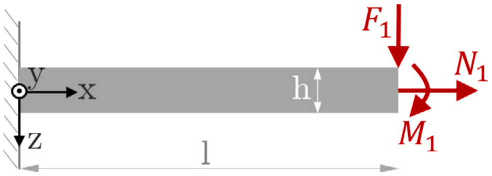

Fig. 6. Cantilever beam of the length l loaded with a lateral force F_1, a moment M_1, and a normal force N_1.

Iosipescu tests [28,29]. As shown by Fedulov, the secant modulus significantly decreases already below 1 % of shear strain [30].

To investigate the sensitivity of the model and the structure of the Jacobian matrix, some additional parameters were considered: the transverse direction modulus E_{22}, Poisson's ratio ν_{12}, the laminate thickness t, as well as the stiffness scaling factors (S_{1E} - S_{4E}) and lateral positions (S_{1y} - S_{4y}) of the four stiffeners.

The selection of calibration parameters was based on an evaluation of the sensitivities obtained from the panel Jacobian matrix. Parameters exhibiting low sensitivity across all measurement locations were excluded from the set of regression parameters for the calibration against experimental data, as their influence on the measured strain field is limited. Including such parameters would reduce parameter identifiability and could potentially lead to unstable updates and a diverging optimization.

4. Results and discussion

The results verify the calibration process and demonstrate the performance and robustness of the proposed algorithm for the stiffened composite panel. First, an analytical beam is considered as a reference for verification. Afterward, the calibration behavior is assessed for synthetic reference data of the stiffened panel, examining convergence and the effect of different parametric deviations. Finally, the Digital Twin is calibrated for an experimental reference in order to create an FE model representing the test specimen as good as possible.

4.1. Verification with an analytical beam example

The verification of the calibration algorithm requires a test case to study the procedure's behavior including the influence of its features like the parameter linearization and the iteratively updated Jacobian matrix. Experimental test cases are mostly too complex and contain too many uncertainties not captured by the calibration parameters.

To subject the calibration procedure to an elementary test, we consider an analytical cantilever beam model as shown in Fig. 6. The beam is subjected to a lateral force F_1, a moment M_1, and a normal force N_1. The beam problem has a closed-form solution. This allows verification of the implementation and its suitability for optimizing the calibration parameters.

The beam deflection w and the axial elongation u under a lateral force F_1, a moment M_1, and a normal force N_1 are given by Eqs. (19) and (20). The curvature κ defined in Eq. (21) follows directly from the deflection. From this curvature and elongation, the axial strain ε_{xx} in the beam is calculated via Equation (23) as a function of the coordinates x and z.

$$w(x) = \frac{F}{6EI}\left(3lx^2 - x^3\right) + \frac{M}{2EI}x^2 \tag{19}$$

$$u(x) = \frac{N_1}{Ehb}x \tag{20}$$

$$\kappa(x) = \frac{F_1}{EI}(l - x) + \frac{M_1}{EI} \tag{21}$$

$$I = \frac{bh^3}{12} \tag{22}$$

$$\varepsilon_{xx}(x, z) = -\kappa(x)\,z + \frac{N_1}{Ehb} \tag{23}$$

The calibration parameters for the beam are the Young's modulus E and the beam thickness h. For the test cases with the parameter linearization outlined in Section 2.4, we invert E and use $E^{-}1$ as a regression parameter, and modify the thickness h, considered as $h^{-}2$ in the calibration. The calibration uses strain measurements at 10 equally spaced locations along the beam length (from $x = 0$ to $x = l$) on both, the upper and the lower beam surfaces with the z-coordinates (at $z = \frac{h}{2}$ and $z = -\frac{h}{2}$, respectively). Fig. 7 depicts the influence of this parameter conversion on the Jacobian matrix and the respective sensitivities which are more balanced for the linearized parameter cases.

The calibration behavior of the beam model is depicted in the diagrams of Fig. 8. Two different initial parameter configurations with −50 % deviation (Guess 1) and 50 % deviation (Guess 2) from the reference values are considered. Each case is calibrated with four different algorithm configurations, with and without parameter linearization and iterative Jacobian updating. Based on the evolution of the calibration parameters, we can examine the convergence of all four configurations for each initial guess.

For Guess 1, all configurations converge. For Guess 2, the calibration diverges when neither linearization nor Jacobian updating is used, and it nearly diverged when the Jacobian is updated but the parameters are not linearized. In contrast, activating linearization stabilized the problem and significantly improves the convergence rate. Iterative Jacobian updating provided an additional benefit but is not sufficient on its own without parameter linearization.

Notably, the linearization of the Young's modulus leads to immediate convergence to its true value for all configurations plotted in Fig. 8. In contrast, the thickness, which cannot be perfectly linearized, requires more iterations to find the true value. In practical terms, reasonable convergence is typically achieved within about five iterations.

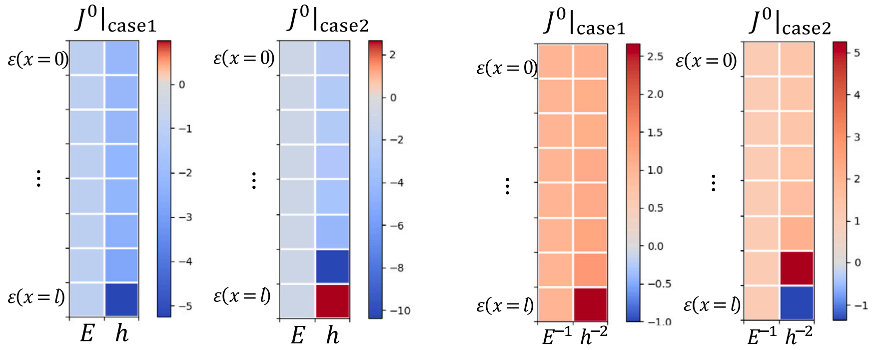

Fig. 7. Jacobian matrices for both initial parameter configurations without linearization (left two) and with linearization (right two).

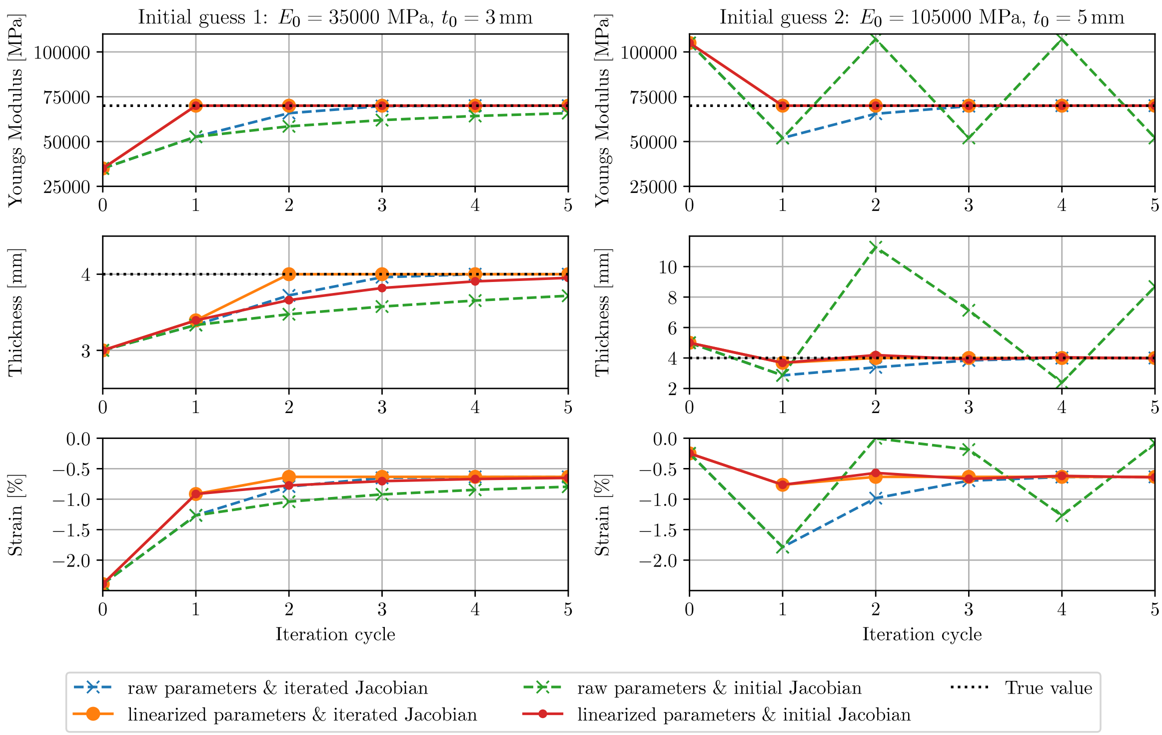

Fig. 8. Calibration of the beam height and the stiffness for an analytical beam model with a true thickness of 4 mm and a modulus of 70 000 MPa.

4.2. Panel calibration with synthetic references

4.2.1. Jacobian matrix of the panel

According to the definition of the Jacobian matrix in Eq. (7), it consists of the gradients of each measurement with respect to each calibration parameter which are replaced by difference quotients in Eq. (8). To obtain these differences for the parameterized FE model, perturbation jobs have to be created, in which one parameter at a time is modified by a predefined perturbation of the regression parameters β_j. For the present example, a step of 3 % was chosen (small enough to remain in the locally linear range, large enough for numerical robustness). Based on the resulting changes in all measurement strains ε_i in the FE model, one column of the Jacobian matrix is obtained by one perturbation j. The accordingly modified Equation (24) defines the Jacobian matrix for the compression panel, where the derivative has been replaced by a difference quotient and the measurements F_i are expressed as strains ε_i.

For the visualization shown in Fig. 9, the matrix is normalized as Eq. (25) shows. Due to the calibration parameter normalization in the denominator, the parameters vanish entirely from the equation, leaving only the perturbation of 3 %.

$$J^0_{i,j} = \left.\frac{\varepsilon_i - \varepsilon^0_i}{\beta_j - \beta^0_j}\right|_{\beta^0} \tag{24}$$

$$J^{0-norm}_{i,j} = \left.\frac{\left(\varepsilon_i - \varepsilon^0_i\right)/\varepsilon^0_i}{\left(\beta_j - \beta^0_j\right)/\beta^0_j}\right|_{\beta^0} = \frac{\varepsilon_i - \varepsilon^0_i}{3\,\% \cdot \varepsilon^0_i} \tag{25}$$

The Jacobian matrix shown in Fig. 9 shows the sensitivity of 30 longitudinal strain measurements to the 17 calibration parameters introduced in Section 3.4. A closer examination of the matrix identifies the parameters which are most significant to the calibration result. High influence is attributed to the longitudinal modulus E_{11}, the shear modulus G_{12}, and the laminate thickness t. Moderate influence was observed for the transverse modulus E_{22}, the rotational clamping stiffness K_r, the imperfections I_1 and $I3$, and for the stiffness and the positions of all four stiffeners. Negligible influence was found for the Poisson's ratio ν_{12} and the imperfection I_2.

Moreover, the presented Jacobian matrix allows for a direct assessment of the parameter identifiability based on the normalized sensitivities. The longitudinal modulus, shear modulus, laminate thickness, and the imperfection amplitudes exhibit the strongest influence

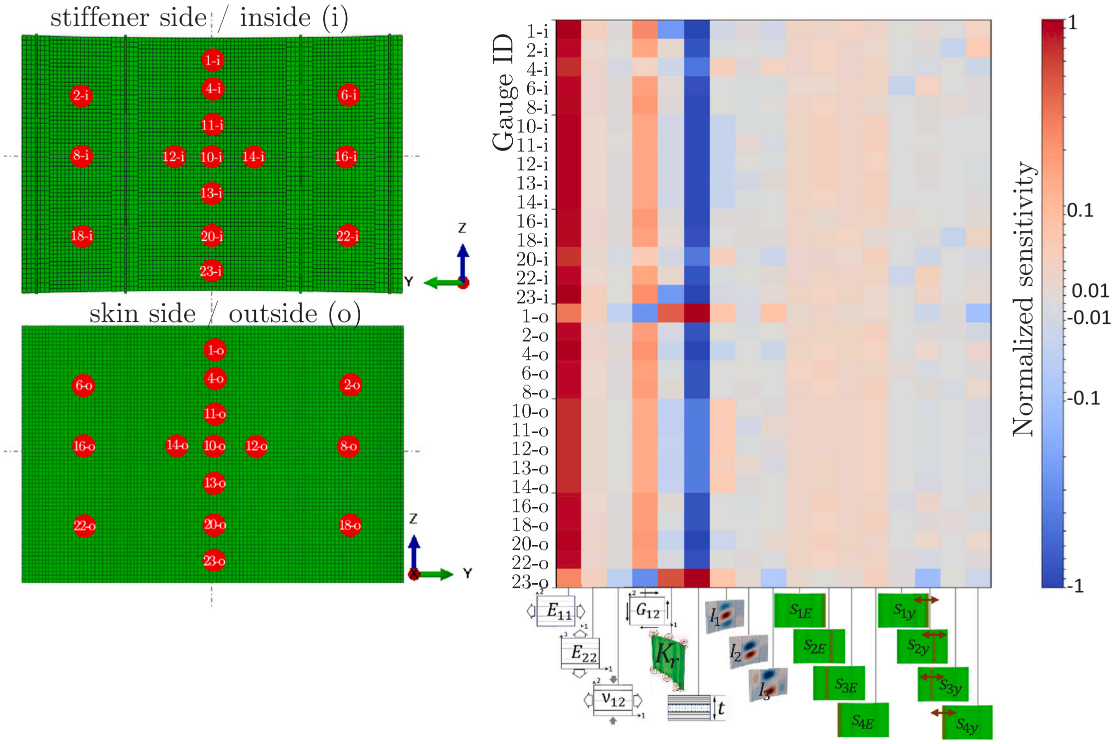

Fig. 9. Normalized Jacobian matrix $J^{0-norm}_{i,j}$ (right) and positions of 30 longitudinal strain gauges (left) for the stiffened compression panel.

on the measured strain field. In contrast, parameters such as the transverse ply stiffness E_{22}, the Poisson's ratio, and the stiffener-related parameters show lower sensitivities in the Jacobian.

Based on these observations, the calibration parameters were selected for the Digital Twin calibration against experimental data. Consequently, parameters with low sensitivity were excluded from the experimental calibration, as their inclusion would likely result in non-physical parameter updates. Still, a synthetic calibration is performed for the stiffener parameters, to evaluate the identifiability of geometric mismatch or local stiffness degradation.

Beyond sensitivity magnitude, the structure of the Jacobian matrix was also examined with respect to potential parameter correlation. Strongly correlated parameters cannot be uniquely identified. For example, a column-wise linear correlation of the longitudinal modulus E_{11} and the laminate thickness t was observed, immediately indicating that both parameters cannot be in the same regression set with the available strain measurements. In comparable manner, a strong correlation between the Poisson's ratio and the shear modulus was observed. The Poisson's ratio with a low sensitivity is, thus, excluded from the regression parameters. Such correlations lead to reduced unique identifiability. For the calibration of a meaningful Digital Twin, only parameters with distinct and sufficiently independent sensitivity patterns were considered, to improve the numerical conditioning of the LSQ problem. Nevertheless, identifiability remains load-case dependent and is limited by the measurement configuration. If additional load cases or measurements were available, the additional parameters could become identifiable.

The method verification and the investigation of its behavior can be most reliably performed against a synthetic reference for the calibration. Such a synthetic reference scenario was constructed by intentionally perturbing selected calibration parameters within the nominal model defining a set $\beta^{ref} \neq \beta^0$. This controlled case allows the observation of the calibration process and the behavior of both measurement and calibration data, verifying the effectiveness and reliability of the developed calibration procedure.

Furthermore, using a synthetic reference allows investigating distinct aspects like the role of the initial parameter set β^0, isolated deviation of each individual calibration parameters, or variations of "unknown" parameters not included in the optimization parameter set β.

4.2.2. Baseline calibration (full measurement set)

A reference case with an initial parameter mismatch was defined according to the expected uncertainty of the respective calibration parameters. The material parameters E_{11} and G_{12} were perturbed by up to 10 % which is slightly above a realistic mismatch for the nominal values. Larger deviations were assigned to the "unknown" parameters: the imperfection amplitudes and to the rotational boundary stiffness. The defined reference parameters differ from the nominal model by more than a factor of two.

The resulting discrepancies between the nominal and the reference strain measurements are approximately ±10 % with up to 40 % for an individual gauge. Two diagrams in Fig. 10 show the evolution of the calibration parameters and the strain measurements throughout the calibration.

The results indicate that already a single LSQ iteration substantially improves the agreement with the reference. An excellent correspondence was achieved after few iterations, which is consistent with the convergence observed for the analytical beam example introduced in Section 4.1. The final result in the form of absolute strains is plotted in Fig. 11. The remaining mismatches are below 1 % for all calibration parameters and for 28 of the 30 strain measurements.

4.2.3. Effect of measurement availability (15 strains)

To investigate the effect of the measurement data availability, the calibration from Section 4.2.2 was repeated using only 15 strains from the outer skin surface of the panel. Fig. 12 shows how this reduction impacts the calibration. While the overall convergence became slower it is also notable that after the first iteration, distinct parameters became worse than in the nominal model (namely G_{12}). Nevertheless, the final result after five iterations featured only minor deviations from the reference below 5 %. The calibration remains useful, but the accuracy is notably worse than the Digital Twin calibrated with the full data set.

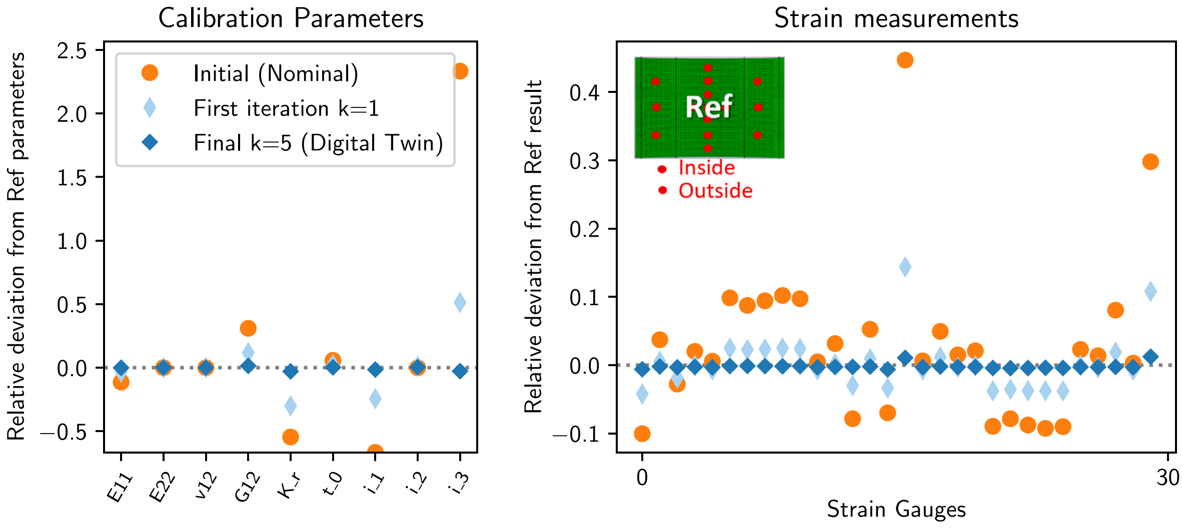

Fig. 10. Normalized calibration results for the compression panel with a synthetic reference simulation. (left: relative deviations of the calibration parameters, right: relative deviation of the strain measurements.).

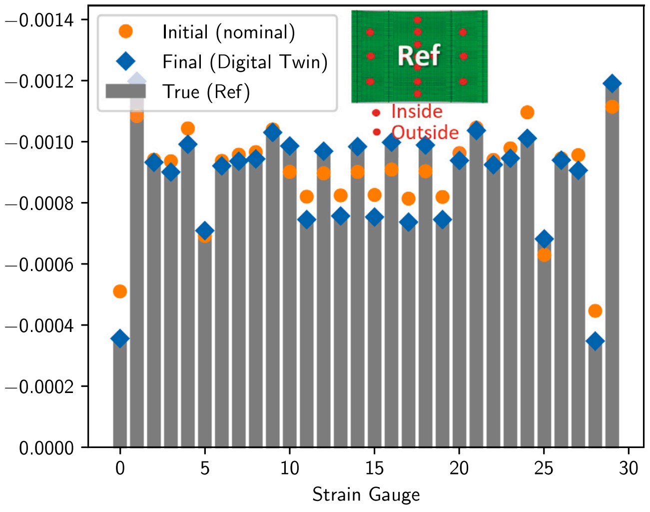

Fig. 11. Strain measurements [$\frac{\text{mm}}{\text{mm}}$] of the nominal model and the Digital Twin compared with the true strain of the synthetic reference simulation.

4.2.4. Perturbations outside the calibration set

Regarding a realistic, experiment-based calibration, a chosen set of calibration parameters cannot reflect all uncertainties present in the nominal model. To consider a scenario with such remaining uncertainty in the synthetic example, we consider an additional synthetic reference simulation in which two additional parameters – E_{22} and t – are subjected to notable perturbations but excluded from the regression. As a consequence, it is not possible to achieve a perfect agreement of the calibration results as Fig. 13 shows. Strain deviations persist in the final optimization result and the estimated parameters match less accurately. Nevertheless, the calibrated Digital Twin remains a notable improvement in comparison to the nominal model.

However, in a real use case, a meaningful calibration requires that the location of degradation is known. For instance, for stiffened CFRP panels guided wave-based damage detection [31,32] and localization can provide the required input to parameterize the stiffness reductions.

4.2.5. Identification of stiffener mismatch and stiffness reduction

The capability of the Digital Twin to detect and localize stiffness reductions is a significant feature explored by different researchers [10–12]. Also the damage detection capability by the presented framework was further explored through targeted investigations, examining a synthetic damage scenario. A damage of one or more stiffeners — represented by scaling parameters introduced to modify the stiffness properties of individual stiffening elements — was studied. Calibration results demonstrated that the Digital Twin methodology reliably identified and quantified stiffness degradation and lateral misalignment in specific stiffeners.

Fig. 14 shows the calibration for a model with perturbations in two stiffening elements. A synthetic reference with a reduced stiffness in stiffener 2 and a 5 mm lateral displacement of stiffener 4 is considered. Both deviations are significant in absolute terms but have only a minor effect on the strain measurements, as the sensitivity of the measurements to these parameters is low compared to other parameters (cf. Jacobian matrix in Fig. 9). Nevertheless, a close match with the reference was achieved through the calibration.

4.3. Panel calibration against an experimental reference

Following the verification using the simulated reference, calibration against actual experimental data was performed using a set of six regression parameters based on the uncertainties presented in Section 3.4. There is no known optimum for the regression parameters. Thus, the calibration quality was assessed solely from the evolution of the strain measurements presented in Fig. 15.

Notably, the nominal model exhibits larger discrepancies ranging between 50 % and 200 % at four individual gauges and systematic discrepancies below 10 % at most other gauges. After the calibration, both the larger outlier and the minor biases were substantially reduced. *The Digital Twin provided a much closer prediction of the experimental reference.*

Fig. 16 reports the relative deviations of each measurement confirming the improvement: even the first iteration (k=1) visibly improved the outliers. The Digital Twin (k=5) additionally exhibits a smaller error in almost all the strain measurements. The diagram depicting the regression parameters in Fig. 16 show the relative evolution of the parameters relative to their nominal values.

Furthermore, the evolution of the residual sum of squares in Eq. (26) over the LSQ iterations serves as an indicator for the progress and the convergence. The *true* residual is calculated from the quadratic deviation of the FE results, the *predicted* residual is the LSQ objective under the local linearization. Due to the model nonlinearity, both residuals initially differ. However, it is clearly visible, that the true

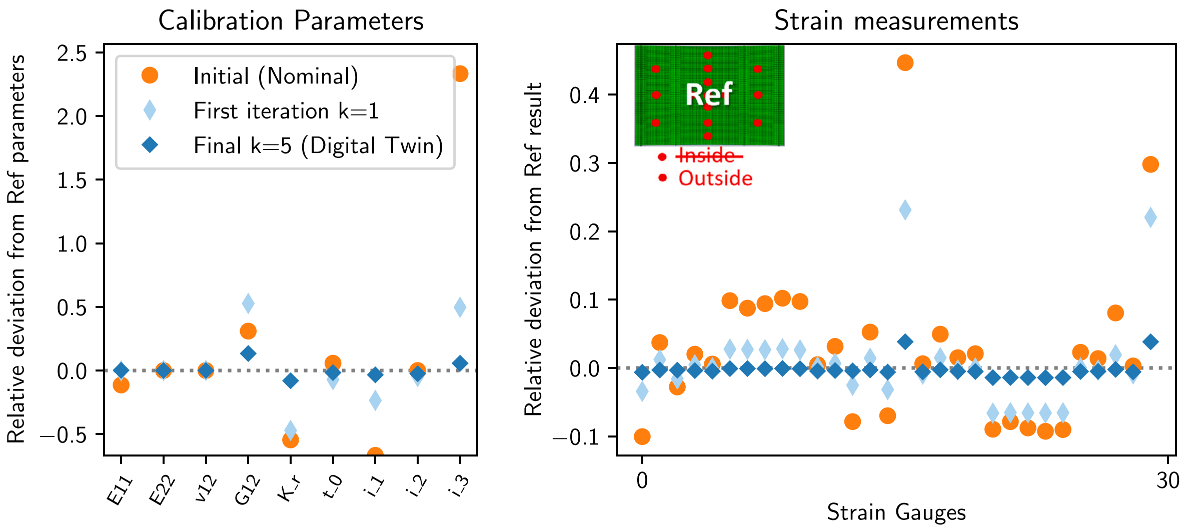

Fig. 12. Normalized calibration results for the compression panel with a synthetic reference simulation where measurement data is only considered from the 15 gauges (measurements 1-15) on the skin side (left: relative deviations of the calibration parameters, right: relative deviation of the strain measurements.).

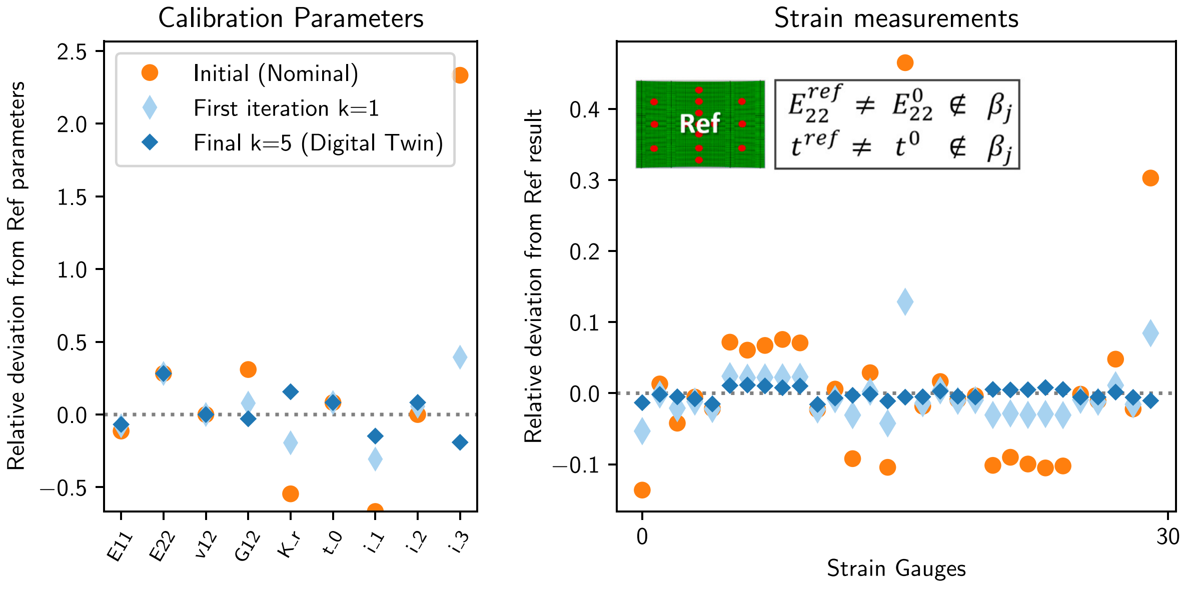

Fig. 13. Calibration results for the compression panel with a synthetic reference simulation. The parameters E_{22} and t are not part of the calibration procedure but exhibit a mismatch between the nominal model and the reference (left: relative deviations of the calibration parameters, right: relative deviation of the strain measurements.).

sum of squared residuals reaches values as low as the expected value, indicating that the constant Jacobian matrix did not compromise the calibration accuracy for this case.

$$R^k = \sum_{i=1}^{m} (y_i^{ref} - F(x, \beta^k)_i)^2 \tag{26}$$

Moreover, the evolution of the residual in Fig. 17 reflects the chosen update strategy (next to the nonlinear response of the FE model). The use of the slowness parameter ξ in Eq. (12), which intentionally reduces the update step to enhance robustness. Selecting $\xi = 1$ would accelerate the convergence and achieve the expected residual through 2 iterations. Nevertheless, the slowness factor improves stability in cases with stronger nonlinearities.

Although full Jacobian recomputation would have been computationally feasible for the present panel model, the constant Jacobian was kept to reflect the intended scalability of the framework toward larger structural models, for which individual nonlinear analyses may require several hours of computation time.

Additional validation was conducted using digital image correlation (DIC) measurements (ARAMIS) which capture the out-of-plane deflection during the compression test. This data was not used in the calibration, and thus provides an independent check for the calibration accuracy. Fig. 18 compares the out-of-plane deflection of the nominal model and the Digital Twin with the ARAMIS measurement from the test, showing that the Digital Twin reproduces the measured deflection better than the nominal model.

It should be emphasized that the DIC measurements were not used during the calibration process. The parameter identification relies exclusively on strain measurements. The comparison of the predicted and measured out-of-plane displacements therefore provides an independent validation of the calibrated model rather than a circular calibration metric.

The calibration results shown in Fig. 16 are summarized quantitatively in Table 2. The optimization found a solution with large updates to the boundary stiffness and imperfections in the order of several hundred percent. It should be noted that the nominal value of

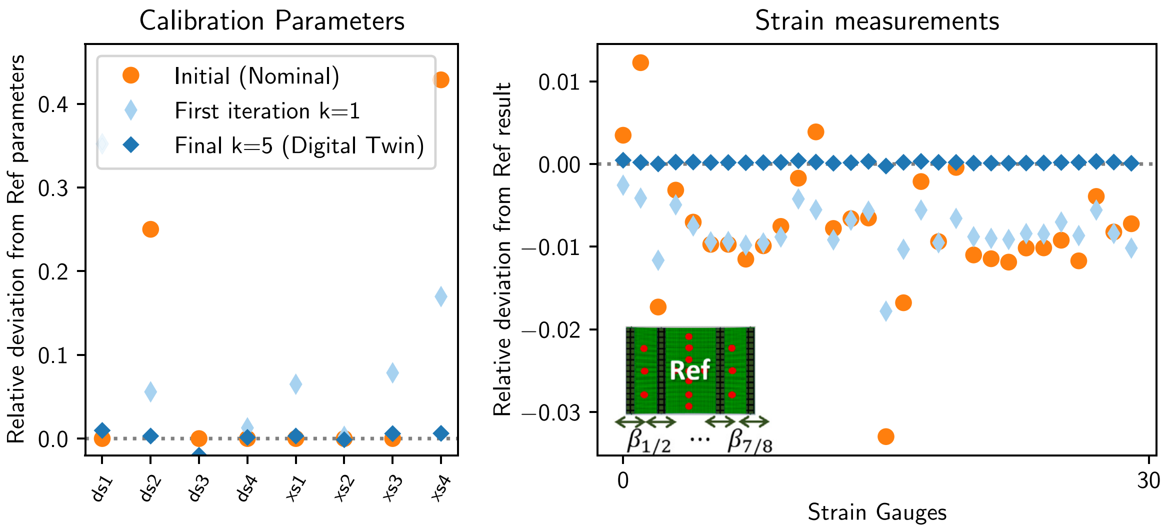

Fig. 14. Normalized calibration results for the compression panel with a synthetic reference simulation with a stiffness loss in stiffener 1 and a 5 mm lateral mismatch of stiffener 4 the reference (left: relative deviations of the calibration parameters, right: relative deviation of the strain measurements.).

Table 2
Calibration results for the compression panel with experimental reference data.

Parameter	Initial (nominal)	Final (Digital Twin)	150 kN Final
E_{11}	156 GPa	167.4 GPa	165.1 GPa
G_{12}	5.50 GPa	4.82 GPa	4.73 GPa
K_{rot}	100 kN mm rad^{-1}	586.5 kN mm rad^{-1}	573.9 kN mm rad^{-1}
Mode I amplitude	1	−0.29	−0.12
Mode II amplitude	1	−1.20	−1.14
Mode III amplitude	1	−0.64	−0.25

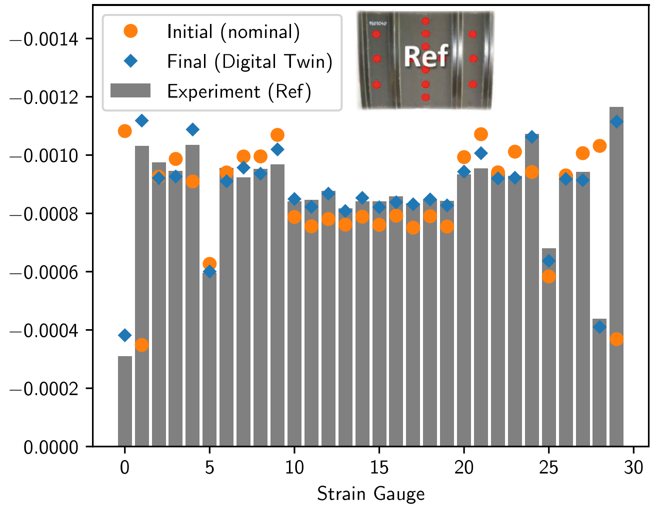

Fig. 15. Strain measurements [$\frac{\text{mm}}{\text{mm}}$] of the nominal model and the Digital Twin compared with the reference strain from a physical test.

both these parameters represent engineering assumptions rather than a measured reference. The observed deviation therefore reflects the correction of initially uncertain estimates of the boundary-condition and the representative imperfection which were based on a limited a priori knowledge.

Minor updates between five and ten percent were found in the optimized stiffness parameters. Both observations are consistent with the expected magnitude of the uncertainties in these parameters.

4.3.1. Discussion of the uncertainties

To complement the point estimates obtained from the calibration, the main sources of uncertainty were assessed using pragmatic sensitivity checks summarized in Table 3.

Calibration-point selection. The choice of the load level used for the calibration point can influence the resulting parameter set. To assess the sensitivity of the calibration to this choice, a second calibration was performed at a load level of 150 kN in addition to the primary calibration at 250 kN. The corresponding results are already reported in Table 2. Notably, the stiffness parameters E_{11}, G_{12}, and K_{rot} exhibit only minor deviations of 1.4 %, 2.3 %, and 2.0 %, respectively. In contrast, the amplitudes of the geometric eigenmode imperfections differ more strongly between both calibrations, reaching 58 %, 5 %, and 61 % for the three modes (all percentages refer to the updated parameter values).

To further assess the validity of the point-based calibration described in Section 2.5, the complete strain histories were evaluated. The comparison of the full strain histories demonstrates that the calibrated parameter set consistently improves the structural response over the entire load range. This additional information allows verification that the Digital Twin represents a physically meaningful model update rather than merely a local curve fit at the selected calibration point. Fig. 19 shows the strain histories for both sides of the skin at all 15 measurement locations.

The strain curves demonstrate that the parameter update improves the strain prediction consistently over the full load range. In particular, at locations such as the top and the bottom of the panel (1-i/1-o and 23-i/23-o, respectively), the Digital Twin reproduces the observed nonlinear strain evolution, whereas the nominal model predicts an almost linear response. This indicates that the updated parameter set captures the governing stiffness characteristics of the structure rather than compensating locally at a single state.

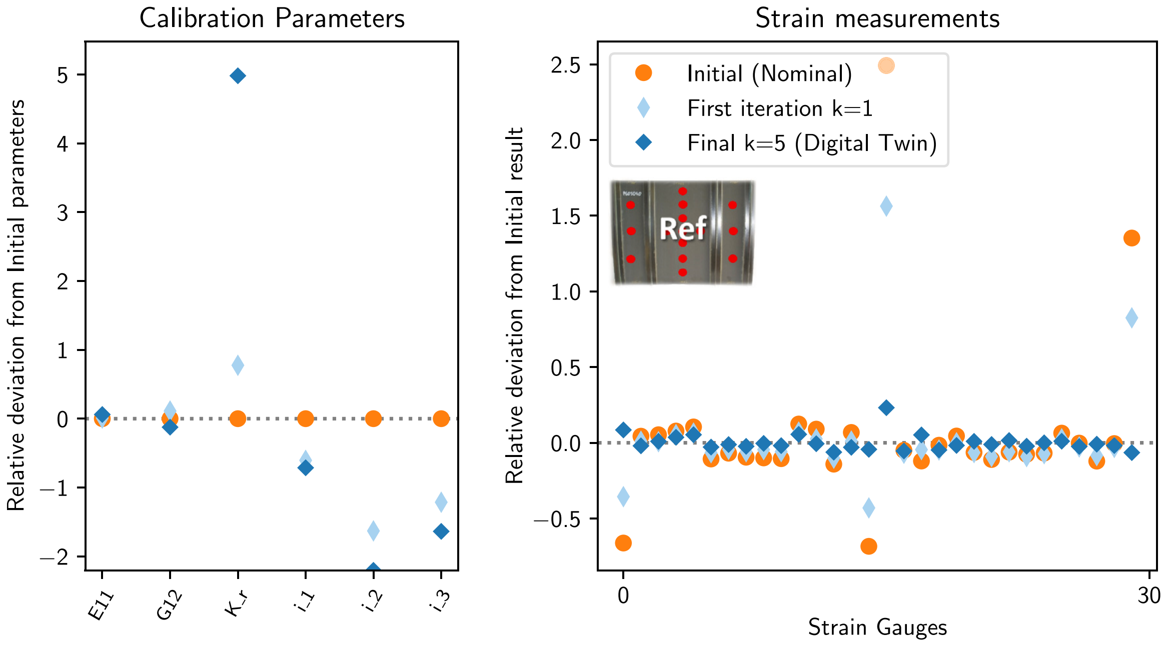

Fig. 16. Normalized calibration results for the compression panel for a physical test. (left: normalized evolution of the calibration parameters, right: relative deviation of the strain measurements.).

Table 3
Primary sources of uncertainty and practical quantification approaches used in this study.

Uncertainty source	Description	Quantification in this work
Calibration load-point selection	A single-point calibration may depend on the selected load level, due to nonlinearities or settling effects	(i) Verification against full strain histories; (ii) calibration at a second load point and comparison of parameter updates.
Measurement set selection	Parameter identifiability and the calibrated solution vary with the coverage of measurement points	Repeated calibrations using different subsets of the full regression set and comparison of residuals and parameter updates.
Parameter estimate uncertainty	Parameter correlations and measurement noise lead to uncertainty in the identified parameter vector under the local linearization.	Linearized LSQ covariance estimate based on $(\mathbf{J}^T\mathbf{J})^{-1}$ scaled by the residual variance (reported as parameter standard deviations/confidence bounds).

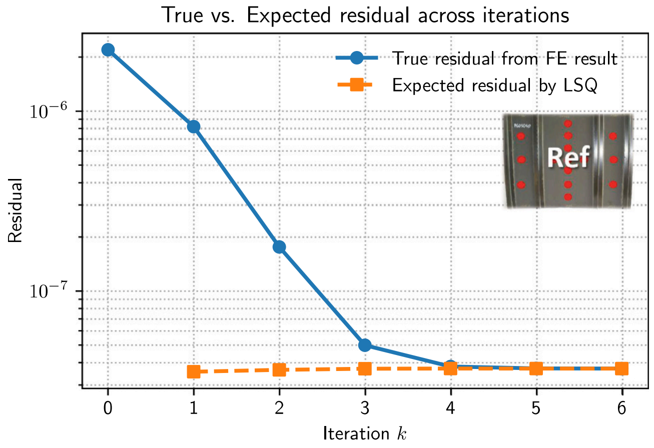

Fig. 17. Evolution of the true sum of squares residuals representing the mismatch of the analysis model and the predicted residual by each nonlinear LSQ optimization cycle.

Nevertheless, a point-based calibration would be insufficient if the structural response exhibited a tipping point, such as the onset of damage growth or structural instability. In such cases, a single calibration point could lead to a non-physical local optimum, and a curve-based or multi-point calibration would be required. For the present panel test, however, the consistency of the strain histories confirms the applicability of the point-based calibration approach.

Measurement set selection. To evaluate the influence of the measurement set on the calibration result, additional calibrations were performed using different subsets of the available measurements. The resulting uncertainty can be assessed by evaluating the prediction accuracy at the remaining measurements that were not included in the calibration subset.

For five randomly selected subsets consisting of 20 measurements each, the deviations of the remaining 10 measurements were compared between the nominal model and the calibrated model. For this subset size, the resulting variability of the calibrated stiffness parameters remained below approximately 9 %, indicating a moderate sensitivity of the parameter estimates to the specific measurement selection. The uncertainty is expected to decrease for a larger measurement set. A quantification for the full measurement set is not possible due to missing control measurements.

Parameter estimate uncertainty. Although the calibration determines the parameter update from a single load point, parameter uncertainty caused by measurement noise can be estimated within the linearized LSQ framework, as explained by Tarantola [33]. Under the assumption of locally linear behavior and independent measurement noise, Tarantola outlines that the covariance of the calibrated parameters can be estimated according to Eq. (27), where σ^2 is calculated from the

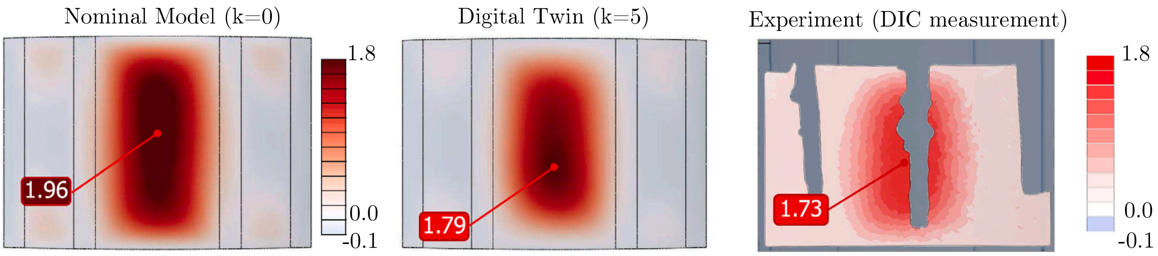

Fig. 18. Out-of-plane displacement [mm] in the nominal model and Digital Twin compared with the ARAMIS measurement from the experiment.

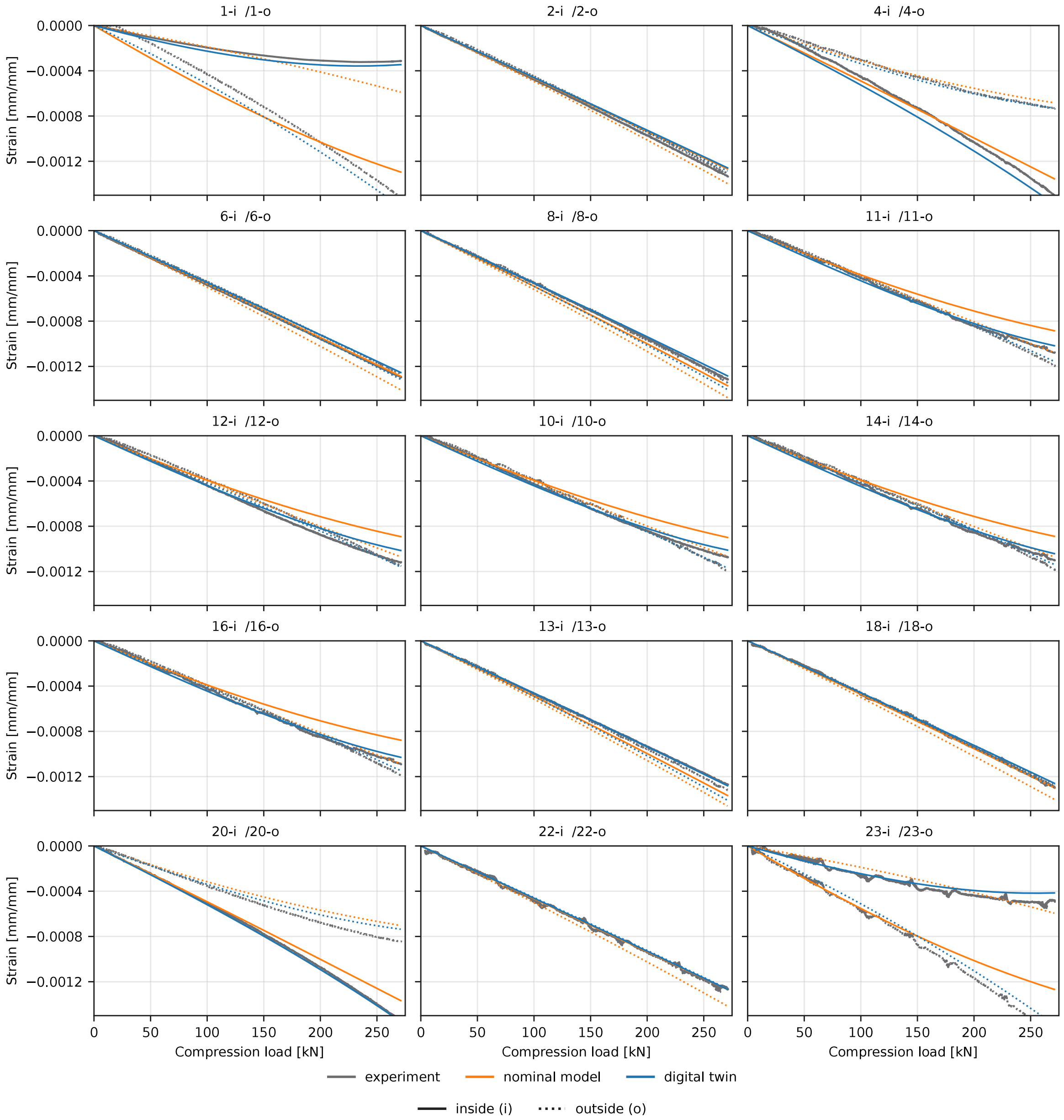

Fig. 19. Strain over axial load for the back-to-back strain gauges at each location on the panel skin (experiment vs. nominal model vs. Digital Twin).

residuals $\frac{\mathbf{r}^T\mathbf{r}}{m-n}$ and J is the Jacobian. This estimate represents a local approximation around the calibrated parameter set.

$$\mathbf{C}_\beta = \sigma^2(\mathbf{J}^T\mathbf{J})^{-1}, \tag{27}$$

In the covariance $\mathbf{C}_\beta$, the individual regression parameter variances are located on the main diagonal. Since stiffness parameters are regressed in transformed form ($\beta_E = \frac{1}{E}$) parameter uncertainties have to be mapped back to the original parameter to enable their physical interpretation. However, the relative uncertainty remains invariant ($\frac{\sigma_E}{E} = \frac{\sigma_{\beta_E}}{\beta_E}$).

Using the covariance estimate, the relative standard deviations of selected calibration parameters were evaluated. For the governing stiffness parameters, the relative uncertainties were found to be 0.0093 for E_{11}, 0.126 for G_{12}, and 3.10×10^{-5} for K_{rot}. These values indicate that the longitudinal stiffness E_{11} and the rotational boundary stiffness K_{rot} are strongly constrained by the available strain measurements, whereas the shear modulus G_{12} exhibits a higher uncertainty. In contrast, the geometric imperfection amplitudes show substantially larger relative uncertainties of 8.66, 3.08, and 7.59 for I_1, I_2, and I_3, respectively. This result reflects that parameters associated with low sensitivity exhibit an increased variance, and, as a consequence, a reduced identifiability. Nonetheless, together with the consistency observed in the full strain histories, this analysis supports the robustness and physical plausibility of the identified parameter set.

5. Conclusion

We presented a nonlinear least squares calibration framework tailored to structural testing, in which a nominal FE model is transformed into a specimen-specific Digital Twin.

Three feature were found critical to an efficient and robust calibration: First, parameter transformations (e.g., $\frac{1}{E_{11}}$ instead of E_{11}) substantially improved the convergence and accuracy of the nonlinear least squares method. Second, point-based calibration with the load as the independent variable avoided biases from compliance of the test machine and clamping equipment. Third, Jacobian-based weighting of the measurements reduced overfitting to weakly sensitive measurements.

The correctness and convergence properties of the calibration method were verified on an analytical beam example and a synthetic compression panel simulation. This allowed direct observation of parameter trajectories throughout the iterative calibration where the remaining mismatches fell below $1\,\%$ for all calibration parameters.

Applied to a compression experiment with a stiffened CFRP panel, the crucial uncertainties in the material properties, the clamping stiffness, and the eigenmode-based imperfection amplitudes were successfully calibrated against strain measurements. Large updates were required for boundary condition stiffness and imperfection amplitudes (order of several hundred percent), whereas material stiffness parameters changed by $5\,\%$ to $10\,\%$). An ARAMIS-based validation of the calibration result confirmed the better predictive accuracy of the Digital Twin.

The robustness of the parameter updates was assessed by evaluating the full strain histories, calibration at an alternative load level, and analyzing the sensitivity to measurement selection and noise. These additional investigations confirm that the identified parameter set represents a physically consistent improvement of the structural model across the entire load range rather than a local fit at the calibration point.

The current version of the calibration framework provides a practical route to more predictive, specimen-specific simulation model — the Digital Twin. Future work will extend the framework to multiple load cases, more complex structures (for example larger stiffened shells, riveted joints, cut-outs). Furthermore, incorporating optical DIC measurement data into the calibration itself could allow replacing local strain information or machine signals, possibly enhancing the calibration on a larger structural scale and requiring less experiment preparation effort.

CRediT authorship contribution statement

Raffael Bogenfeld: Writing – original draft, Visualization, Validation, Methodology, Investigation, Funding acquisition, Formal analysis, Data curation, Conceptualization. **Tobias Wille:** Writing – review & editing, Supervision, Project administration, Investigation, Funding acquisition, Conceptualization. **Oliver Witzel:** Visualization, Validation, Resources, Investigation, Data curation, Conceptualization. **Benjamin Eckstein:** Writing – review & editing, Supervision, Project administration, Methodology, Investigation, Funding acquisition, Conceptualization. **Christian Göpel:** Supervision, Project administration, Investigation, Conceptualization.

Declaration of competing interest

The authors declare the following financial interests/personal relationships which may be considered as potential competing interests: Raffael Bogenfeld reports financial support was provided by Federal Ministry for Economic Affairs and Energy (BMWE). Benjamin Eckstein reports financial support was provided by Federal Ministry for Economic Affairs and Energy (BMWE). Oliver Witzel reports financial support was provided by Federal Ministry for Economic Affairs and Energy (BMWE). If there are other authors, they declare that they have no known competing financial interests or personal relationships that could have appeared to influence the work reported in this paper.

Acknowledgments

The authors acknowledge the Federal Ministry for Economic Affairs and Energy (BMWE) of Germany for funding the LuFo VI-2 research project Rapid EF Enablers (FKZ: 20D2105 A (Airbus), 20D2105D (ZEISS), 20D2105G (DLR)) and all partners of this joint research project. All work related to this article was accomplished within this project.

Data availability

Data will be made available on request.

References

[1] J. Rouchon, Certification of large airplane composite structures, ICAS, in: Proceedings of the 17th Congress of the International Council of the Aeronautical Sciences, vol. 2, Stockholm, Sweden, 1990, pp. 1439–1447, URL https://icas.org/icas_archive/ICAS1990/ICAS-90-1.8.1.pdf.

[2] F. Vetrano, P. Worton, H. Smaoui, A. Szukala, S. Thukaram, A. Al-Logmani, A. Alyazidi, S. Green, M. Halsall, P. Montagnon, L. Sahbatou, A.-L. Simon, F. Donati, E. Galli, G. Stilo, P. Herbillon, B. Haberkorn, S. Kremer, A. Bergstrom, J. Hagelin, B. Brault, Y. Delga, A.-C. Lemine, G. Mabboux, Recommendations on increased use of modelling and simulation for certification / qualification in aerospace industry, in: AIAA SCITECH 2024 Forum, American Institute of Aeronautics and Astronautics, Orlando, FL, USA, 2024, http://dx.doi.org/10.2514/6.2024-1625.

[3] P. Linde, J. Pleitner, W. Rust, Virtual testing of aircraft fuselage stiffened panels, in: Proceedings of the 24th Congress of the International Council of the Aeronautical Sciences, ICAS, Yokohama, Japan, 2004, pp. 1–9, URL https://icas.org/icas_archive/ICAS2004/PAPERS/255.PDF.

[4] M. Shafto, M. Conroy, R. Doyle, E. Glaessgen, C. Kemp, J. LeMoigne, L. Wang, Draft Modeling, Simulation, Information Technology & Processing Roadmap, Technology Area 11, National Aeronautics and Space Administration (NASA), Washington, DC, USA, 2010, pp. 1–32, URL https://www.researchgate.net/publication/280310295_Modeling_Simulation_Information_Technology_and_Processing_Roadmap.

[5] M. Grieves, Digital Twin: Manufacturing Excellence Through Virtual Factory Replication, White Paper, Michael W. Grieves LLC, Melbourne, FL, USA, 2014, pp. 1–7, URL https://www.researchgate.net/publication/275211047_Digital_Twin_Manufacturing_Excellence_through_Virtual_Factory_Replication.

[6] M. Grieves, Origins of the digital twin concept, 2016, http://dx.doi.org/10.13140/RG.2.2.26367.61609, Working paper, Researchgate, Florida Institute of Technology, Melbourne, FL, USA, URL https://www.researchgate.net/doi/10.13140/RG.2.2.26367.61609.

[7] M. Singh, E. Fuenmayor, E.P. Hinchy, Y. Qiao, N. Murray, D. Devine, Digital twin: Origin to future, Appl. Syst. Innov. 4 (2) (2021) http://dx.doi.org/10.3390/asi4020036.

[8] M. Xiong, H. Wang, Digital twin applications in aviation industry: A review, Int. J. Adv. Manuf. Technol. 121 (9–10) (2022) 5677–5692, http://dx.doi.org/10.1007/s00170-022-09717-9.

[9] D. Jones, C. Snider, A. Nassehi, J. Yon, B. Hicks, Characterising the digital twin: A systematic literature review, CIRP J. Manuf. Sci. Technol. 29 (Virtual) (2020) 36–52, http://dx.doi.org/10.1016/j.cirpj.2020.02.002.

[10] Z. Huang, X. Yin, Y. Liu, Y. Liu, Damage identification of truss bridges based on feature transferable digital twins, Measurement 233 (2024) 114735, http://dx.doi.org/10.1016/j.measurement.2024.114735.

[11] H. Habbouche, Y. Amirat, T. Benkedjouh, M. Benbouzid, Digital twin-based gearbox fault diagnosis using variational mode decomposition and dynamic vibration modeling, Measurement 246 (2025) 116669, http://dx.doi.org/10.1016/j.measurement.2025.116669.

[12] Q. Li, G. Zhao, J. Li, S. Li, W. Yan, X. Tian, S. Ai, An in-situ predictive method for modulus degradation in composite structures with fatigue damage: Applications in digital twin technology, Mech. Syst. Signal Process. 237 (2025) 113090, http://dx.doi.org/10.1016/j.ymssp.2025.113090.

[13] R. Bogenfeld, Calibration of a digital twin for structural testing, in: 11th International Conference on Composite Testing and Model Identification (CompTest), Universitat de Girona. Grup de Recerca en Anàlisi i Materials Avançats per al Disseny Estructural (AMADE), Girona, Spain, 2023, URL https://elib.dlr.de/197023/.

[14] L. Li, S. Aslam, A. Wileman, S. Perinpanayagam, Digital twin in aerospace industry: A gentle introduction, IEEE Access 10 (2022) 9543–9562, http://dx.doi.org/10.1109/access.2021.3136458.

[15] Å. Björck, Least squares methods, Handb. Numer. Anal. 1 (1990) 465–652, http://dx.doi.org/10.1137/1.9781611977950.

[16] J. Fox, S. Weisberg, Nonlinear Regression, Nonlinear Least Squares, and Nonlinear Mixed Models in R: An Appendix to An R Companion to Applied Regression, Third Ed., McMaster University, Hamilton, ON, Canada, 2018, URL https://socserv.socsci.mcmaster.ca/jfox/books/companion/appendices/Appendix-Nonlinear-Regression.pdf. Last revision: 2018-06-02.

[17] M. Pourahmadi, Taylor expansion of and some applications, Am. Math. Mon. 91 (5) (1984) 303–307, http://dx.doi.org/10.1080/00029890.1984.11971411.

[18] H.A.L. Kiers, Weighted least squares fitting using ordinary least squares algorithms, Psychometrika 62 (2) (1997) 251–266, http://dx.doi.org/10.1007/BF02295279.

[19] Hexcel, HexPly M91 Product Data Sheet, Hexcel Corporation, Stamford, CT, USA, 2020, URL https://www.hexcel.com/wp-content/uploads/2025/12/HexPly_M91_global_DataSheet.pdf. (Accessed: 18 March 2026).

[20] C.P. Dienel, Damage Assessment for Composite Structures based on Individual Residual Strength Prediction (Ph.D. thesis), Technische Universität Carola-Wilhelmina zu Braunschweig, Braunschweig, Germany, 2019, URL https://elib.dlr.de/134178/.

[21] R. Bogenfeld, A combined analytical and numerical analysis method for low-velocity impact on composite structures (Ph.D. thesis), Technische Universität Carola-Wilhelmina zu Braunschweig, Braunschweig, Germany, 2019, URL https://elib.dlr.de/130241/.

[22] D. Wilckens, R. Degenhardt, K. Rohwer, R. Zimmermann, M. Kepke, B. Hildebrandt, A. Zipfel, Cyclic buckling tests of pre-damaged CFRP stringer-stiffened panels, Int. J. Struct. Stab. Dyn. 10 (4) (2010) 827–851, http://dx.doi.org/10.1142/S0219455410003762.

[23] R. Degenhardt, A. Kling, R. Zimmermann, F. Odermann, F. de Araújo, Dealing with imperfection sensitivity of composite structures prone to buckling, in: S.B. Coskun (Ed.), Advances in Computational Stability Analysis, IntechOpen, London, 2012, http://dx.doi.org/10.5772/45810.

[24] Carl Zeiss G.O.M. Metrology GmbH, 3D testing – optical 3D measurement of strain, deformation and displacement, 2025, Braunschweig, Germany, URL https://www.zeiss.com/metrology/en/systems/optical-3d/3d-testing.html. (Accessed: 13 March 2025).

[25] M. Ismail, J. Purbolaksono, A. Andriyana, C. Tan, N. Muhammad, H. Liew, The use of initial imperfection approach in design process and buckling failure evaluation of axially compressed composite cylindrical shells, Eng. Fail. Anal. 51 (2015) 20–28, http://dx.doi.org/10.1016/j.engfailanal.2015.02.017.

[26] S.G. Castro, R. Zimmermann, M.A. Arbelo, R. Khakimova, M.W. Hilburger, R. Degenhardt, Geometric imperfections and lower-bound methods used to calculate knock-down factors for axially compressed composite cylindrical shells, Thin-Walled Struct. 74 (2014) 118–132, http://dx.doi.org/10.1016/j.tws.2013.08.011.

[27] A.C. Orifici, C. Bisagni, Perturbation-based imperfection analysis for composite cylindrical shells buckling in compression, Compos. Struct. 106 (2013) 520–528, http://dx.doi.org/10.1016/j.compstruct.2013.06.028.

[28] ASTM D 5379 Standard Test Method for Shear Properties of Composite Materials by the V-notched Beam Method no. March, ASTM International, West Conshohocken, PA, USA, 2005, http://dx.doi.org/10.1520/D5379_D5379M-19E01, URL https://astm.org/d5379_d5379m-19e01.html.

[29] G. Odegard, M. Kumosa, Determination of shear strength of unidirectional composite materials with the iosipescu and 10 off-axis shear tests, Compos. Sci. Technol. 60 (16) (2000) 2917–2943, http://dx.doi.org/10.1016/S0266-3538(00)00141-X.

[30] B. Fedulov, A. Fedorenko, A. Safonov, E. Lomakin, Nonlinear shear behavior and failure of composite materials under plane stress conditions, Acta Mech. 228 (6) (2017) 2033–2040, http://dx.doi.org/10.1007/s00707-017-1817-4.

[31] S. Sikdar, W. Ostachowicz, A. Kundu, Deep learning for automatic assessment of breathing-debonds in stiffened composite panels using non-linear guided wave signals, Compos. Struct. 312 (2023) 116876, http://dx.doi.org/10.1016/j.compstruct.2023.116876.

[32] I. Mueller, V. Memmolo, K. Tschöke, M. Moix-Bonet, K. Möllenhoff, M. Golub, R.S. Venkat, Y. Lugovtsova, A. Eremin, J. Moll, Performance assessment for a guided wave-based SHM system applied to a stiffened composite structure, Sensors 22 (19) (2022) 7529, http://dx.doi.org/10.3390/s22197529.

[33] A. Tarantola, Inverse Problem Theory and Methods for Model Parameter Estimation, SIAM, Philadelphia, PA, USA, 2005, http://dx.doi.org/10.1137/1.9780898717921, URL https://epubs.siam.org/doi/book/10.1137/1.9780898717921.